Synergistic regulation of charge state and electron-donating ability via heterojunctions design for fixation of electronegative greenhouse F-gases

Xiang Meng [a,b,1], Boxu Dong [a,1], Liang Zhao [a], Wenhui Zhou [a], Xinhao Li [a], Jiantao Zai [a,c,*], Xuefeng Qian [a]

[a] *Shanghai Electrochemical Energy Devices Research Center, School of Chemistry and Chemical Engineering and Shaoxing Research Institute of Renewable Energy and Molecular Engineering, Shanghai Jiao Tong University, Shanghai 200240, PR China*
[b] *Department of Chemistry, City University of Hong Kong, 999077, Hong Kong, China*
[c] *Key Laboratory of Green and High-End Utilization of Salt Lake Resources, Chinese Academy of Sciences, Qinghai 810008, PR China*

ARTICLE INFO

ABSTRACT

The net-zero greenhouse gas emission has now become a global strategy. In this context, electronegative fluorinated-gases such as sulfur hexafluoride (SF_6) and hydrofluorocarbon, have become important emission reduction objects due to their strong global warming potential. In this work, the MnOx@Mn/SiC heterojunction was rationally designed and prepared. Because of the high electron coupling, the positively charged active-site MnOx@Mn (δ^+) not only promotes the adsorption of SF_6 but also acts as a donor to transport electrons to SF_6, so that the adsorption and activation of SF_6 are unified in one active site. Therefore, MnOx@Mn/SiC can effectively degrade SF_6 above 450°C, and the degradation amount for 12 vol% SF_6 can reach 523.8 mL g^{-1} at 600°C. Furthermore, it also has good degradation performance on hydrofluorocarbons (R-22 and R-410A) even at 100°C. Given the cheap and easy scale-up synthesis, MnOx@Mn/SiC has the potential to reduce the emission of multiple fluorinated-gases in practical applications.

1. Introduction

In the past few decades, the greenhouse effect has posed a huge threat to the sustainable development of human society, so the net-zero greenhouse gas emission has become a global strategy. Besides well-known CO_2, multiple electronegative fluorinated-gases (F-gases), represented by sulfur hexafluoride (SF_6) and hydrofluorocarbon (HFC) are very strong greenhouse gases due to their extremely high global warming potential, which is more than thousands of times CO_2 equivalent [1,2]. Currently, global F-gases emissions exceed one billion tons of CO_2 equivalent per year, which has become an urgent environmental issue.

For instance, SF_6 has the highest global warming potential of 23,900 CO_2 equivalent, and the concentration of SF_6 in the global atmosphere increased from less than 0.04×10^{-12} L/L in 1953 to ~10.0×10^{-12} L/L in 2020 [3–5]. The emission of SF_6 in China is expected to reach 116 million tons of CO_2 equivalent in 2030 [6]. Currently, the leaked low-concentration SF_6 is often emitted directly into the air (<1000 ppm)

[7–10]. Complete degradation is a more suitable fixation strategy for low-concentration SF_6 compared with concentration and purification process [11–15]. However, it is still a formidable challenge to achieve efficient degradation of SF_6 on catalysts due to the extreme inertia of SF_6 molecules [16].

Given the strong electronegativity of F, heterostructures with uneven electron distribution can promote the adsorption of SF_6 on positively charged active sites [17–21]. On the other hand, in the activation of SF_6 and HFCs, F is not a good leaving group in most cases due to the unique inertia of the S-F bond and the C-F bond [22,23]. Generally, constructing active sites with strong Lewis acid effect can promote the activation and functionalization of some fluorinated organic compounds by accepting electrons from F atoms [24–26]. However, the activation of stable F-gases always follows a reduction process. According to the molecular orbital theory, the non-bonding orbital is the highest electron occupied orbital of SF_6 molecules, and is fully filled. Injecting electrons into the anti-bonding orbital of SF_6 can reduce its bond order (Scheme 1). The reduction of SF_6 could be facilitated on electron-donating active sites.

Thus, the interfacial synergistic mechanism between adsorption and activation sites is very important, which has been demonstrated on the rectified SiC-Fe$_2$O$_3$ heterostructures [27]. However, such adsorption and activation of SF$_6$ must be realized in separate sites and request good cooperation between electron donor and acceptor.

The integration of the adsorption and reduction of SF$_6$ onto one active site will be a possible idea to further promote the fixation of SF$_6$. To realize this proposal, the positively charged active site should have the ability to offer electrons. However, it is difficult to continuously make the positively charged site as an electron donor. One shortlist is to use the self-oxidation of metal site with a low valence state to constantly provide electrons during the fixation of SF$_6$ (Scheme 1).

Most of the catalysts that have been commercially used to degrade volatile organic compounds and other pollutants are noble-metal-based materials [28,29]. Although these materials have excellent degradation performance and long degradation lifetime, the high price is always the main disadvantage restricting the large-scale commercial application. In contrast, non-noble transition metals have gradually attracted more attention because of their cheap price, earth-abundant, low preparation cost, and environmental friendliness [30,31]. Among them, Mn is a promising active center due to its variety of variable valence states, which is conducive to electron transfer and heterojunction regulation [32,33]. Xia and co-workers reported that α-MnO$_2$ with abundant oxygen vacancy can achieve efficient catalytic ozonation of CH$_3$SH [34]. (310) facets have a higher surface energy and a high concentration of oxygen vacancies than other facets, thus promoting adsorption and activating O$_3$ as the active intermediates to eliminate CH$_3$SH. However, no work has been reported that Mn-based materials can be used to degrade SF$_6$. Silicon carbide (SiC), meanwhile, is a wide band gap (~3.2 eV) semiconductor with excellent thermal conductivity and chemical stability, so it is widely used as a catalyst support [35,36]. When combined to form the heterojunction, Mn species (MnOx@Mn) will be positively charged (δ$^+$) and can facilitate adsorption and degradation of SF$_6$ molecules [37]. Therefore, a MnOx@Mn/SiC heterojunction was designed and fabricated via a simple ball milling process. The formation of positively charged reductive sites was systematically characterized. Such designed sites can promote the adsorption of electronegative SF$_6$, and realize the low-temperature reductive fixation of this strongest greenhouse gas. The degraded temperature can lower to 450 °C and the maximum degradation amount can reach 523.8 mL g^{-1} in this work. In addition to SF$_6$, MnOx@Mn/SiC also has excellent degradability to HFCs (R-22 and R-410A) even at low temperatures.

2. Experimental section

2.1. Sample preparation

Mn and SiC were purchased from Shanghai Titan Scientific Co., Ltd, and SF$_6$ was acquired from Shanghai Weichuang Standard Gas Co., Ltd. Descriptions of other chemicals and materials were provided in Support Information.

The MnOx@Mn/SiC heterojunction was prepared by ball milling with the Pulverisette 6 Planetary Mono Mill. Take a certain amount of SiC and Mn for preliminary grinding in an agate mortar, and control the ratio of SiC and Mn to 4:1. Then the agate balls were mixed in the agate tank with a mass ratio of 1:10. Fasten the agate tank and mill it for 3 h at a speed of 300 r/min. The sample was washed with DI water and dried in the vacuum oven at 80 °C for 12 h, and then placed in a mortar and ground manually for 5 min. The MnOx@Mn/SiC heterojunction was obtained.

Keep the total amount of composites 2.5 g and the proportion of Mn element in composites 20 wt% unchanged, a variety of Mangan-based composites with different electronic structures of active centers, such as SiC/MnO(II), SiC/Mn$_2$O$_3$(III), SiC/MnO$_2$(IV) can be obtained by changing the valence states of such active centers as MnO, Mn$_2$O$_3$ and MnO$_2$.

2.2. Sample characterization

The concentration of SF$_6$ was decected by gas chromatography (GC 7900), and its detector is the thermal conductivity detector (TCD). The crystal structure was resolved by X-ray diffractometer (XRD, Shimadzu XRD-6100) using Cu Kα radiation (λ = 0.154178 nm) at 40 mA and 40 kV.

In-situ XRD tests were performed in the high temperature reaction cell manufactured by In-situ High-tech to track the phase evolution during the reaction process. Generally, about 0.1 g of sample was placed in the reaction cell and heated to 600 °C with reaction gas at a flow rate of 10 mL min^{-1}. The temperature of the reaction cell was controlled within ± 0.5 °C of set point, and the pressure was maintained at 0.1 MPa during the reaction.

The morphology of the sample was characterized by scanning electron microscopy (SEM, Nova NanoSEM 450) with an accelerating voltage of 10 kV. The energy dispersive X-ray spectroscopy (EDX) results were obtained by the FEI Talos F200X at 200 kV. The inductively-coupled-plasma-optical-emission-spectroscopy (ICP-OES) was operated
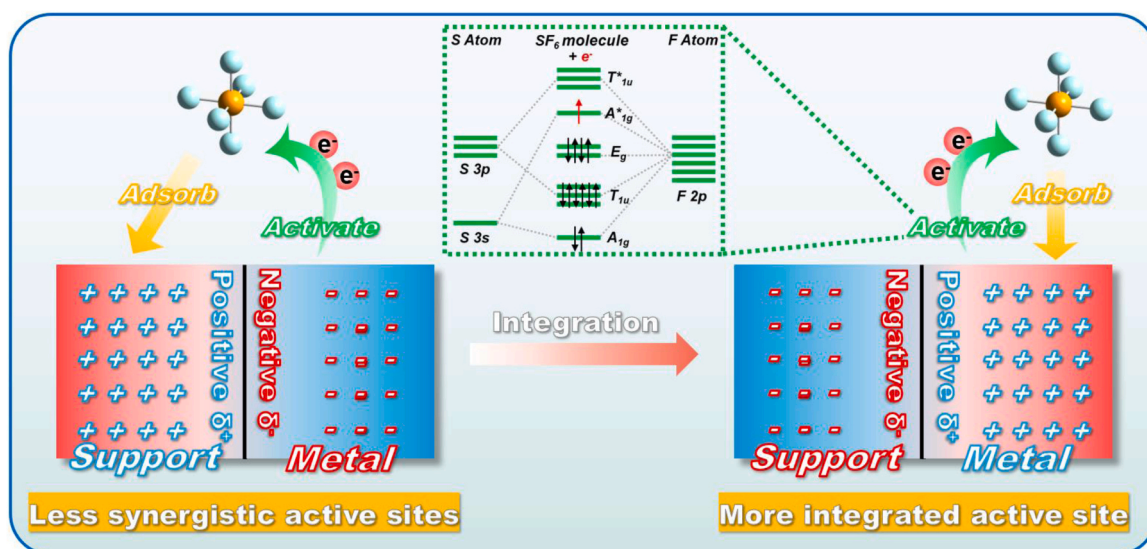
Scheme 1. The activation of SF$_6$ on MnOx@Mn/SiC heterojunction; a positively charged reductive active site.

by Avi500. The microstructure of the sample was analyzed by transmission electron microscopy (TEM, FEI Talos F200X) running at 200 kV. The valance and electronic structure of the sample were obtained by X-ray photoelectron spectroscopy (XPS, AXIS Ultra DLD), using Al Kα as light source. Record the adsorption and desorption capacity of the sample with Chemisorption Apparatus (VDsorb-91i) and analyze it by temperature programmed desorption (TPD). TPD mode used SF_6 for preadsorption treatment, and Helium (He) for purging.

2.3. SF₆ degradation testing

The degradation performance of the sample was evaluated by a heating reaction bed device. Place 2.5 g prepared sample in a quartz tube with 8 mm inner diameter and block both ends of it with quartz wool. Put the quartz tube in the tube furnace and set the corresponding temperature. Typically, the sample was pre-activated in reaction gas flow at room temperature for 15 min before the reaction. 3 vol% SF_6 (the ratio of SF_6 to air: 3:97) at a flow rate of 10 mL min^{-1} was used in most of the following tests, and the relative humidity of the air is around 50%. In addition, by changing the concentration (3 vol%, 6 vol%, 9 vol % and 12 vol%) and flow rate (5 mL min^{-1}, 10 mL min^{-1}, and 20 mL min^{-1}) of the reaction gas, the influence of these factors on the reaction process was explored. After the reaction, the tail gas was absorbed with 5 M NaOH solution. The concentration of SF_6 in the tail gas was analyzed by GC. The calculation method of the SF_6 conversion is shown in the Supporting Information.

2.4. DFT calculations

The DFT calculation was performed by using plane-wave basis sets on Materials studio. In order to optimize both MnO, SiC, SF_6 and MnOx@Mn/SiC structures, the exchange correlation function, PBE generalized gradient approximation with Koelling–Hamon relativistic treatment, and spin polarization assumption are employed. Broyden–Fletcher–Goldfarb–Shanno geometry optimization is used for cell optimization. The interaction between valence electrons and the ionic core are described by using On-The-Fly-Generation ultra soft pseudo potential. To generate highly accurate electrochemical stability diagrams, we employ a recently developed approach which includes use of a Hubbard U term to correct for self-interaction errors in the ultrathin films. The kinetic cutoff energy for convergence test is 600 eV, and a k-point set mesh ($2 \times 2 \times 1$) parameter is used for Brillouin zone sampling. The threshold for self-consistent field iterations used is 1.0×10^{-6} eV atom^{-1}. The convergence tolerance parameters of the optimized calculation are the tolerance for energy 1.0×10^{-5} eV atom^{-1}, the maximum force of 0.03 eV Å^{-1}, and maximum displacement of 1×10^{-3} Å. The vacuum space along the Z direction is 20 Å to prevent the effect of the adjacent atomic slabs.

3. Results and discussions

3.1. Construction of positively charged active sites

In order to degrade SF_6, the MnOx@Mn/SiC heterojunction was prepared by ball milling (Fig. S1). Firstly, the crystal structure of MnOx@Mn/SiC was characterized by XRD patterns. By comparing with the standard pattern of pure SiC and Mn, a strong diffraction peak was retrieved at 43.0° in the MnOx@Mn/SiC heterojunction (Fig. S2), which corresponds to the (411) crystal plane of Mn (PDF no.01–089-2412). The remaining main peaks are consistent with (101), (102), (006), (104), (105), (107), and (110) crystal planes of SiC (PDF no.01–074-1302). Then the morphology and structure of MnOx@Mn/SiC were further verified by SEM and TEM (Fig. 1a-c). SiC exists in block form, and the small particle of Mn is available on the surface of SiC (Fig. S3). From TEM mapping (Fig. 1a), it is more intuitive to prove the existence of SiC and Mn, and the fusion of the two-phase interface can also be observed
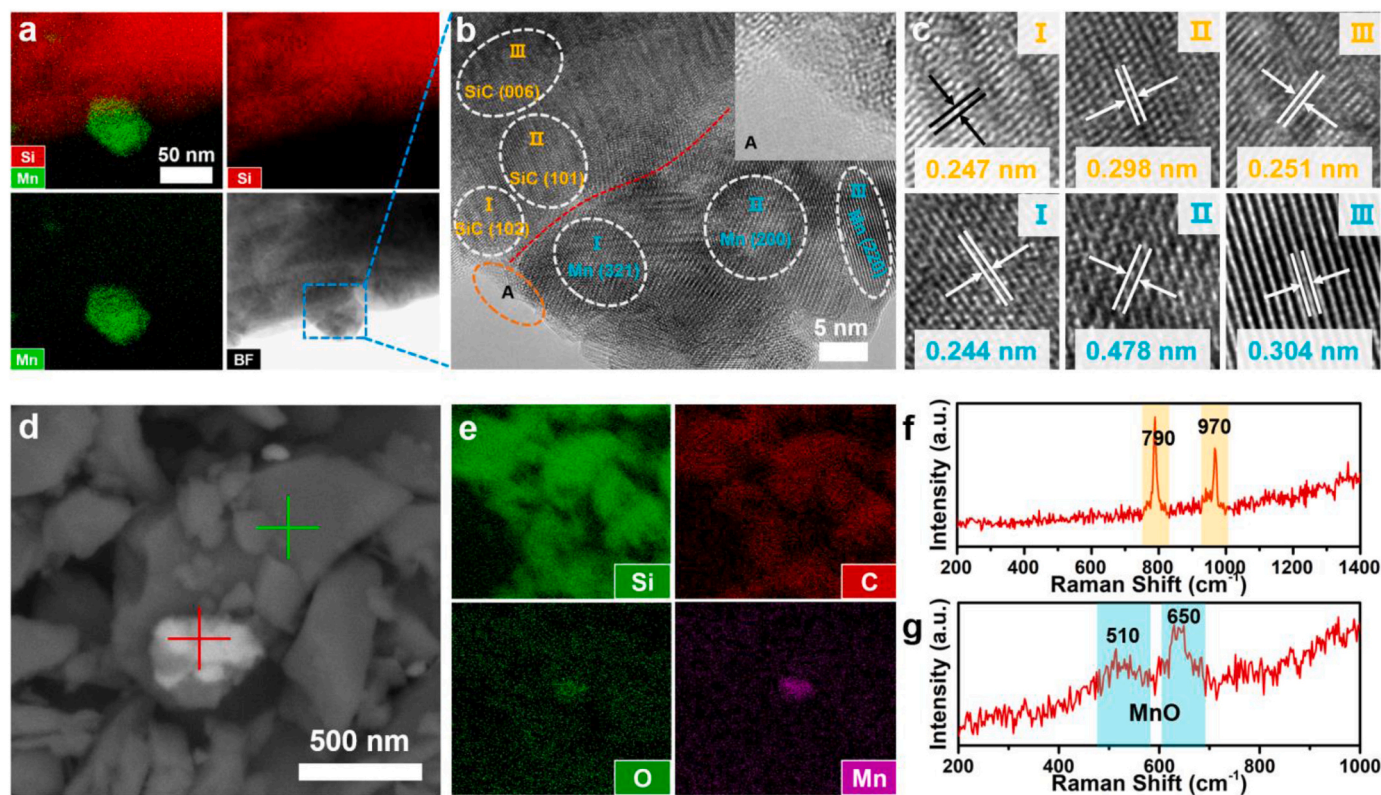

Fig. 1. a) TEM elemental mapping images, b-c) HRTEM images in the box area of a); d) BSE image, e) EDX elemental mappings of MnOx@Mn/SiC; f) Raman spectrum taken from the green-crisscross spot in the BSE image of d), g) Raman spectrum taken from the red-crisscross spot of MnOx@Mn/SiC.

in the box area, which was further analyzed by HRTEM images (Fig. 1b-c). The interplanar spacings of 0.247 nm, 0.298 nm, and 0.251 nm can be observed, which corresponds to the (102), (101), and (006) crystal planes of SiC. At the same time, the interplanar spacings of 0.244 nm, 0.478 nm, and 0.304 nm can be well-indexed to the (321), (200), and (220) crystal planes of Mn (Fig. 1c). The formation of MnOx@Mn/SiC heterojunction can be confirmed by clear lattice fringes and two-phase interface[38,39]. In addition, amorphous layers were found at the interface of MnOx@Mn/SiC and the surface of crystal phase, as shown in inset A of Fig. 1b. The proportion of Mn element measured by ICP and EDX is 19.90 wt% and 17.74 wt%, respectively (Table S1).

The Raman imaging scanning electron (RISE) microscope was used to characterize the surface properties of MnOx@Mn/SiC. The bright spot in Fig. 1d shows Mn particles, while the dark background is SiC. The element distribution was further determined through EDX mapping (Fig. 1e, S4). Firstly, Raman spectral point-analysis was performed on dark background, and the peaks at 790 cm^{-1} and 970 cm^{-1} were highly consistent with the SiC (Fig. 1f). The Raman spectrum at the bright spot was shown in Fig. 1g, and the peaks at 510 cm^{-1} and 650 cm^{-1} could be retrieved as MnO. The weak peak intensity of the Raman spectrum proves that the crystallization of MnO is very poor. This strongly verifies the amorphous layer observed from HRTEM (Fig. 1b) and explains why no MnO was detected by XRD pattern (Fig. S2).

In order to further prove that the MnOx@Mn/SiC is not a simple mixture of SiC and Mn, but a heterojunction formed at the interface, the electronic interaction and valence states of samples were investigated by XPS (Fig. 2)[40,41]. From the full spectra, O 1 s, Si 2p, and Mn 2p peaks are detected simultaneously in the MnOx@Mn/SiC heterojunction (Fig. 2a). Compared with pure Mn, the content of O-Lattice in the high-resolution O 1 s XPS spectrum of the MnOx@Mn/SiC heterojunction is greatly reduced (Fig. 2b). At the same time, the surface of MnOx@Mn/SiC has a relatively higher content of O-adsorbed[42], which combines with SiC to form Si-O bonds after ball milling.

In the deconvoluted Mn 2p XPS spectrum of the MnOx@Mn/SiC heterojunction, there are five peaks (Fig. 2c). The paired peaks at 641.4/652.9 eV and 643.7/654.7 eV are assigned to the MnO and MnO_2,

respectively. The peak located at 647.0 eV can be corresponded to satellite feature of MnO. Compared with pure Mn, the Mn^{2+}/Mn^{4+} molar ratio of MnOx@Mn/SiC reduced from 2.48 to 1.68, which means that the average valence state of the composites increases (Table S2). More importantly, Mn^{2+} $2p_{3/2}$ in the MnOx@Mn/SiC heterojunction positively shifts about 0.2 eV, which shows that Mn as an electron donor transfers electrons to SiC. The electron transfer can be further proved by Si 2p spectra. From Fig. 2d, the Si 2p spectrum of the MnOx@Mn/SiC heterojunction is deconvoluted into two peaks at 100.2 and 102.3 eV, corresponding to Si-C and Si-O. Compared with SiC, Si-O of MnOx@Mn/SiC has a negative shift of 0.2 eV. This strongly shows that SiC accepts electrons from Mn as an electron acceptor, which proves the formation of the MnOx@Mn/SiC heterojunction. Moreover, the relative content of the Si-O bonds increased significantly (Table S2), indicating that the SiC was partially reduced to SiO in the space charge region of the heterojunction.

At the same time, charge transfer at the interface of the MnOx@Mn/SiC heterojunction was further rationalized via the computational method, see Fig. 2e. The calculated charge-density difference shows that the charge on the Mn atom is partially transferred to the surface of the Si atom after the combination of MnOx@Mn and SiC[43], leading to the Mn oxidation and Si reduction, which is in good agreement with XPS results. Because of the uneven distribution of electrons, the positively charged MnOx@Mn species is more conducive to adsorbing the strongly electronegative SF_6 molecules.

3.2. Efficient adsorption and activation of SF_6 on the MnOx@Mn/SiC heterojunction

Herein, we used a high-temperature reaction device to verify the degradability of SF_6 on MnOx@Mn/SiC heterojunction (Fig. S5). The sample was placed in the reaction bed to degrade 3 vol% SF_6, and the mass flowmeter was used to control the flow rate.

Compared with pure Mn and MnOx@Mn/SiC, when the temperature reaches 600 °C, the SF_6 degradation ratio on SiC is always 0, which means that pure SiC has no degradability at all. The initial degradation
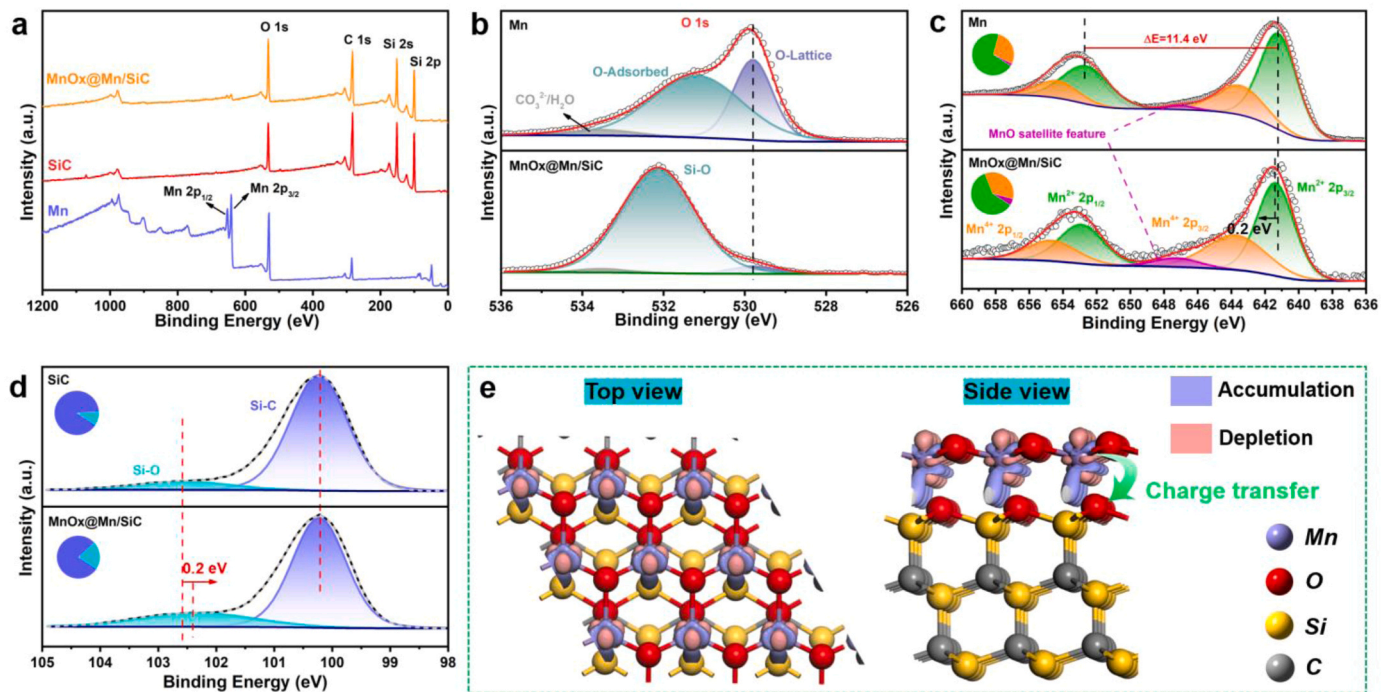

Fig. 2. a) XPS full spectra of SiC, Mn, and MnOx@Mn/SiC heterojunction; b) High-resolution O 1 s XPS spectra, c) Mn 2p XPS spectra of Mn and MnOx@Mn/SiC; d) High-resolution Si 2p XPS spectra of SiC and MnOx@Mn/SiC; e) Charge-density differences at the interface of the MnOx@Mn/SiC heterojunction (isosurface: 0.1 a. u.). Purple indicates electron accumulation while light coralline shows electron depletion.

ratio (degradation ratio at 0 min) on pure Mn is 53%. Then it shows a downward trend and loses its degradability after 40 min (Fig. S6). Moreover, the degradation amount is also an indicator to measure the degradation performance of the sample, and the degradation amount of SF_6 by the Mn is only 3.8 mL g^{-1} (Fig. 3a). The initial degradation ratio of MnOx@Mn/SiC is 78%, and the degradation ratio reaches 100% after 30 min. In addition, the degradation amount has also been greatly improved, which is 81.2 mL g^{-1}.

SF$_6$-TPD was used to characterize the adsorption capacity of different samples for SF_6 (Fig. 3b). For SiC, the first peak located at 220 °C could be attributed to physisorption and the second peak that appears at 526 °C originates from chemisorption of SF_6. For Mn, there is one typical tall peak at 700 °C owing to the desorption of the gas-phase product SO_2 formed during the reaction. On this basis, the two high-temperature peaks at 608 °C and 680 °C of MnOx@Mn/SiC can be attributed to the chemisorption of SF_6 on the SiC carrier and the desorption of SO_2 on the active site. The three weak peaks in the middle-temperature region (472 °C, 518 °C, and 537 °C) may be from the physisorption of multiple phases in the composites. The detailed peak evolution of SF$_6$-TPD spectra shows that the desorption peak of SF_6 on MnOx@Mn/SiC shifted to high temperature, while the desorption peak of SO_2 shifted to low temperature compared to the single-phase sample, which proves that the

adsorption of SF_6 on MnOx@Mn/SiC was enhanced, while the adsorption of SO_2 was inhibited, promoting the forward movement of chemical equilibrium[43].

Based on the optimized model, DFT calculation was used to study the surface charge transfer and the adsorption process between SF_6 and SiC, MnO, and MnOx@Mn/SiC heterojunction (Fig. 3c-f)[44,45]. The adsorption energy of SF_6 on SiC was 0.11 eV, which indicates that pure SiC is not easy to adsorb SF_6. Compared with MnO, the construction of MnOx@Mn/SiC heterojunction can enhance the adsorption of SF_6 with the decreased adsorption energy from -0.43 eV to -0.62 eV, contributing to efficient adsorption and activation of SF_6 molecules (Fig. 3c, S7).

In addition, by comparing several Mangan-based composites with different valence states, it can be found that these composites are ranked as follows according to their degradation amounts of SF_6: SiC/Mn(0) > SiC-MnO(II) > SiC-Mn$_2$O$_3$(III) > SiC-MnO$_2$(IV) composites, as shown in Fig. S8. The degradation performance for SF_6 decreased with the increase of the valence state of Mn species. This is because the increase of the valence state of the same species means the decrease of reducibility. For a reductive system such as SF_6 degradation, a strong reductive active center can provide electrons to SF_6 molecules continuously, which is more conducive to the breaking of S-F bonds.
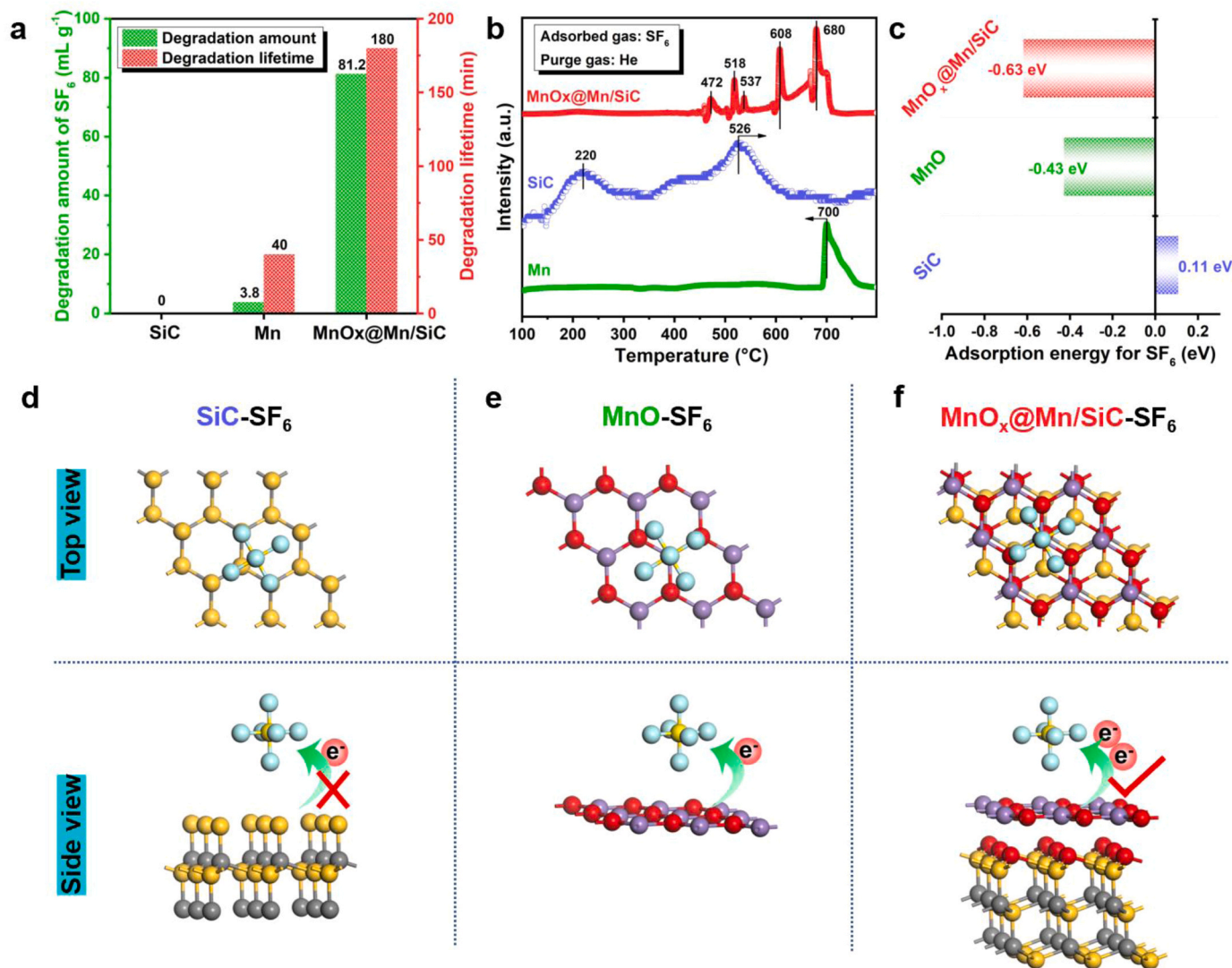

Fig. 3. a) Degradation activity of SF_6 on SiC, Mn, and the MnOx@Mn/SiC heterojunction under a flow rate 10 mL min^{-1} 3 vol% SF_6 at 600 °C; b) TPD spectra of SF_6 adsorption on the surfaces of SiC, Mn, and MnOx@Mn/SiC heterojunction; c) Adsorption energy for SF_6 on SiC, MnO, and MnOx@Mn/SiC; Surface charge transfer and the adsorption process between SF_6 and d) SiC, e) MnO, f) MnO$_x$ @Mn/SiC heterojunction.

3.3. Proposed mechanism of SF₆ degradation over MnOx@Mn/SiC heterojunction

In-situ XRD was used to characterize the active-phase evolution of MnOx@Mn/SiC during the heating process (Fig. 4). Generally, 0.1 g of sample was placed in the high-temperature reaction cell (Fig. S9) and heated to 600 °C with 3 vol% SF_6 at a flow rate of 10 mL min⁻¹. Fig. 4b is the setting of the heating program. The reaction cell was heated by 20 °C within 1 min, and then kept at this temperature for 9 min, resulting in a series of XRD patterns. In Fig. 4a, the sample has obvious phase changes in three angle ranges. For example, Fig. 4e represents area. It is found that when rising to ~420 °C, the main peak of Mn located at 43.0° gradually decreases, which proves that Mn element was first oxidized at high temperature before reacting with SF_6.

When it rises to 450 °C, two diffraction peaks at 32.5° and 38.5° gradually appear in Fig. 4c-d, which are consistent with the main peak of Mn_2O_3. Moreover, it can be seen from Fig. 5a that the lowest temperature at which MnOx@Mn/SiC could exert degradation performance is 450 °C. Therefore, the transformation of MnO into Mn_2O_3 is the main reaction process related to the SF_6 degradation.

Take out the sample that the degradation ratio just reached 100% at 600 °C for XPS characterization, and the sample is defined as MnOx@Mn/SiC (reacting). From Fig. 4f-g, the Mn^{2+} $2p_{3/2}$ peak of MnOx@Mn/SiC (reacting) continues to shift positively by 0.2 eV relative to the Mn^{2+} $2p_{3/2}$ of MnOx@Mn/SiC (fresh), which proves that the heterojunction acts as an electron donor in the reaction. In the process of SF_6 gaining electrons, the S-F bond is gradually activated, forming SF_5, SF_4, SF_3, and so on. Finally, the gas phase product SO_2 is formed.

However, there is no obvious Mn^{3+} peak in the XPS of MnOx@Mn/SiC (reacting), and we believe that this can be attributed to the ex-situ characterization of XPS. In the process from obtaining the sample to taking the characterization, Mn^{3+} is reduced by Mn element to Mn^{2+}. This explains why, despite a positive shift in Mn^{2+} $2p_{3/2}$ of MnOx@Mn/SiC (reacting), the molar ratio of Mn^{2+}/Mn^{4+} has increased from 1.68 to 2.02 (Table S2).

The sample that completely lost activity after degradation at 600 °C is defined as MnOx@Mn/SiC (deactivated). It is found that Mn^{2+} $2p_{3/2}$ of MnOx@Mn/SiC (deactivated) continues to have a positive shift, and the molar ratio of Mn^{2+}/Mn^{4+} is further increased to 2.90 (Table S2). It shows that the Mn element is almost completely converted to Mn^{2+} when the reaction is deactivated. From several new XRD diffraction peaks gradually appearing above 450 °C in Fig. S10, it can be seen that Mn^{2+} mainly exists in the form of $MnSiO_3$ (PDF no.00–012-0181). During the reaction with SF_6, the Si-O bond peak of MnOx@Mn/SiC continues to positively shift, which is opposite to the shift during the formation of the heterojunction (Fig. 4h). When deactivated, SiO was almost oxidized to SiO_2/SiO_3^{2-}. Furthermore, by comparing the in-situ XRD patterns of pure SiC during the heating process, we confirmed that pure SiC does not undergo the obvious phase transition at high temperature (Fig. S11).

In short, due to the uneven electron distribution in the heterojunction, we believe that MnOx@Mn (δ^+) can promote the adsorption of SF_6 inspired by the negatively charged F. In the meantime, MnOx@Mn, acting as an electron donor, can transfer electrons to SF_6 and be further oxidized to Mn_2O_3 (Fig. 4i). Mn^{3+} can be reduced to Mn^{2+} by Mn element (or by the synergistic effect of oxidation of SiO), which promotes the continuous degradation of SF_6. Through such a positively charged reductive active site, the intrinsic catalytic activity of MnOx@Mn/SiC heterojunction is greatly enhanced.

However, with the increase of SiO_3^{2-} generated during the destruction of SF_6, SiO_3^{2-} was deposited on the Mn^{2+} active site to form $MnSiO_3$ and covered the surface of MnOx@Mn/SiC. Silicates have no SF_6 degradation effect, which is the main factor causing the deactivation of MnOx@Mn/SiC heterojunction. Herein, we performed an interesting experiment where the deactivated sample was taken out and re-ground. After testing, the deactivated sample still had the degradability (Fig. S12).

3.4. Degradation performance of electronegative F-gases

Next, to explore the degradation performance of MnOx@Mn/SiC under different experimental conditions, a series of experiments were processed (Fig. 5). First, we tested the effect of reaction temperature (Fig. 5a-c). Below 400 °C, there is no degradation effect at all. MnOx@Mn/SiC can exert its degradability at 450 °C, and the highest degradation ratio can reach 53% (Fig. 5a). Compared with the reported work, this is the lowest temperature at which SF_6 can be degraded (Table S3). At 550 °C, MnOx@Mn/SiC achieved 100% degradation for the first time. The degradation lifetime has also been extended. When the reaction temperature is increased to 600 °C, the 100% degradation ratio can last for 80 min. At 600 °C, GC was used to check the SF_6 concentration in the exhaust every 10 min, thereby obtaining a series of GC signals (Fig. 5b). When the retention time is 0.8 min, it is the peak of N_2, and the peak of SF_6 appears at 1.7 min. It can be clearly seen that from 30 to 110 min, there is almost no SF_6 peak. After 120 min, the peak area of SF_6 gradually increases, indicating that the degradation ratio is getting lower. By 180 min, the peak area is the same as that of the original gas (3 vol% SF_6), which proves that MnOx@Mn/SiC has been deactivated.

In addition, the degradation amount at 600 °C (81.2 mL g⁻¹) is twice as high as that at 550 °C (40.0 mL g⁻¹), and it is clear that the degradation amount increases consistently with the increase of reaction temperature (Fig. 5c). Since our goal is to study the lowest temperature at which SF_6 can be degraded and to find a more energy-efficient degradable material, we do not explore the degradation performance above 600 °C.

Besides, Mn content of MnOx@Mn/SiC has a great influence on the degradation performance (Fig. 5d, S13). 20 wt% Mn has the highest degradation amount, compared with other contents (5 wt%, 10 wt%, 30 wt%, and 40 wt%). The low Mn content means the lack of active sites, which is not conducive to giving full play to the degradation performance of MnOx@Mn/SiC. However, when the Mn content is too high, it leads to overlap of active sites, and also affects the synergistic effect between the carrier and active sites. In conclusion, it is very important to choose a suitable dispersion to improve the degradation performance.

Flow rate also affects degradation performance. The slower the flow rate, the higher the degradation amount of SF_6, up to 106.4 mL g⁻¹ at 5 mL min⁻¹ (Fig. S14). This can be attributed to the sufficient adsorption of SF_6 on the MnOx@Mn/SiC heterojunction. XRD patterns under different flow rates show no significant phase changes (Fig. S15). It is also worth noting that the degradation performance of MnOx@Mn/SiC improves with increasing SF_6 concentration (Fig. S16). At 12 vol%, the degradation amount of SF_6 can reach 523.8 mL g⁻¹, which is 6.5 times of that at 3 vol% (Fig. 5e). And this is the highest in all experiments of this work (Table S5). This indicates that the reaction of Mn with SF_6 and the oxidation in air are in competition.

In addition, the degradation ability of the MnOx@Mn/SiC heterojunction for two other electronegative gases, R-22 ($CHClF_2$) and R-410A ($50\%CH_2F_2/50\%CF_3CHF_2$), was also investigated (Fig. 5f). It is worth noting that R-22 and R-410A are refrigerants commonly used today and have a strong greenhouse effect[46,47], similar to SF_6. The results show that R-22 can be effectively degraded below 200 °C, even at 100 °C. It is worth noting here that such a low temperature degradation process can effectively avoid the formation of dioxins[48]. Similarly, MnOx@Mn/-SiC also has the ability to degrade R-410A at a low temperature of 100 °C. Therefore, the MnOx@Mn/SiC heterojunction system proposed in this work has universal and efficient degradation performance for a variety of electronegative gases.
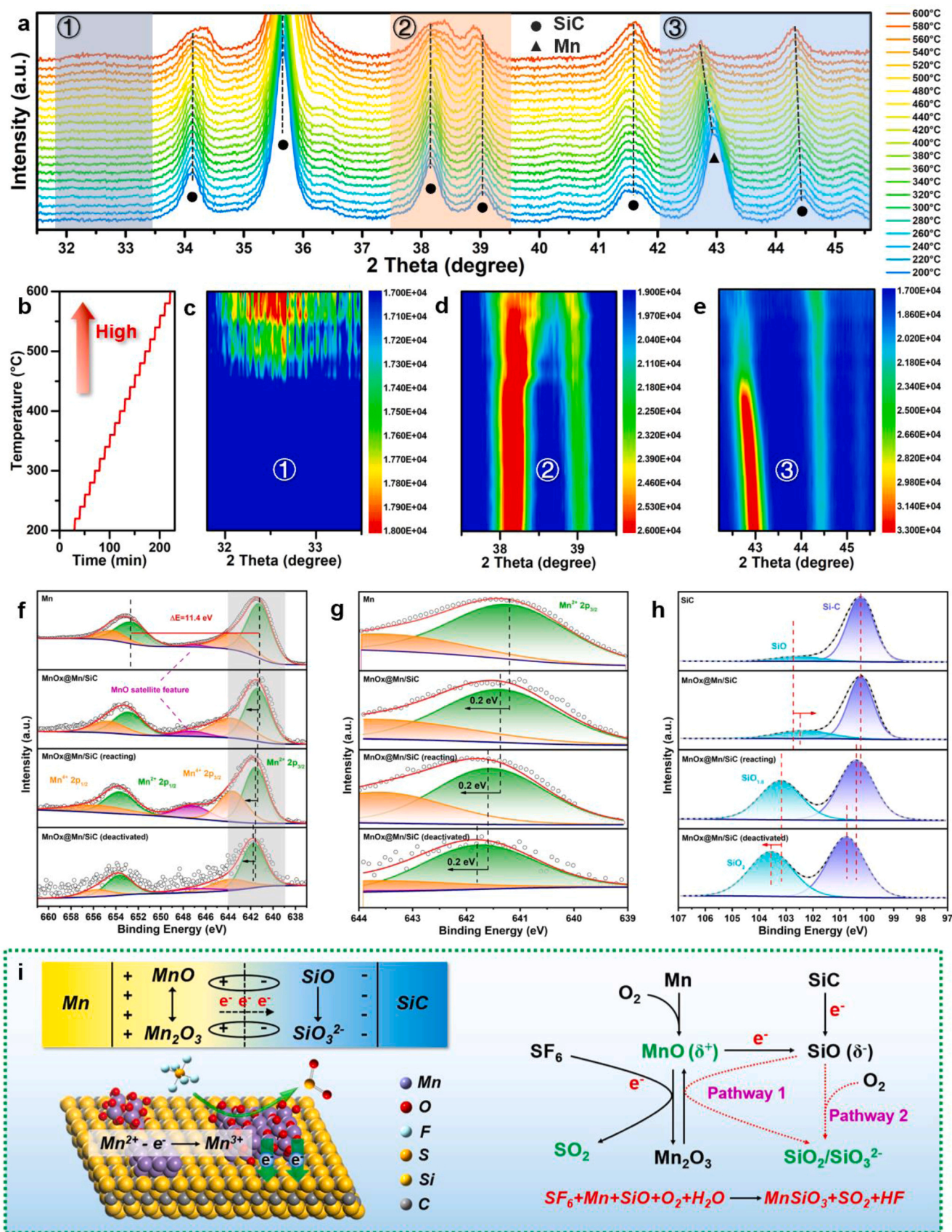
Fig. 4. a) In-situ XRD patterns of the MnOx@Mn/SiC heterojunction during heating (up to 600 °C); b) Setting of the heating program for in-situ XRD test; XRD patterns in the c) area ①, d) area ②, e) area ③ of a). f) High-resolution Mn 2p XPS spectra of Mn, MnOx@Mn/SiC, MnOx@Mn/SiC (reacting) and MnOx@Mn/SiC (deactivated). g) XPS spectra in the gray area (644–639 eV) of f); h) High-resolution Si 2p XPS spectra of SiC, MnOx@Mn/SiC, MnOx@Mn/SiC (reacting) and MnOx@Mn/SiC (deactivated); i) Reaction mechanism involved in the SF$_6$ degradation.
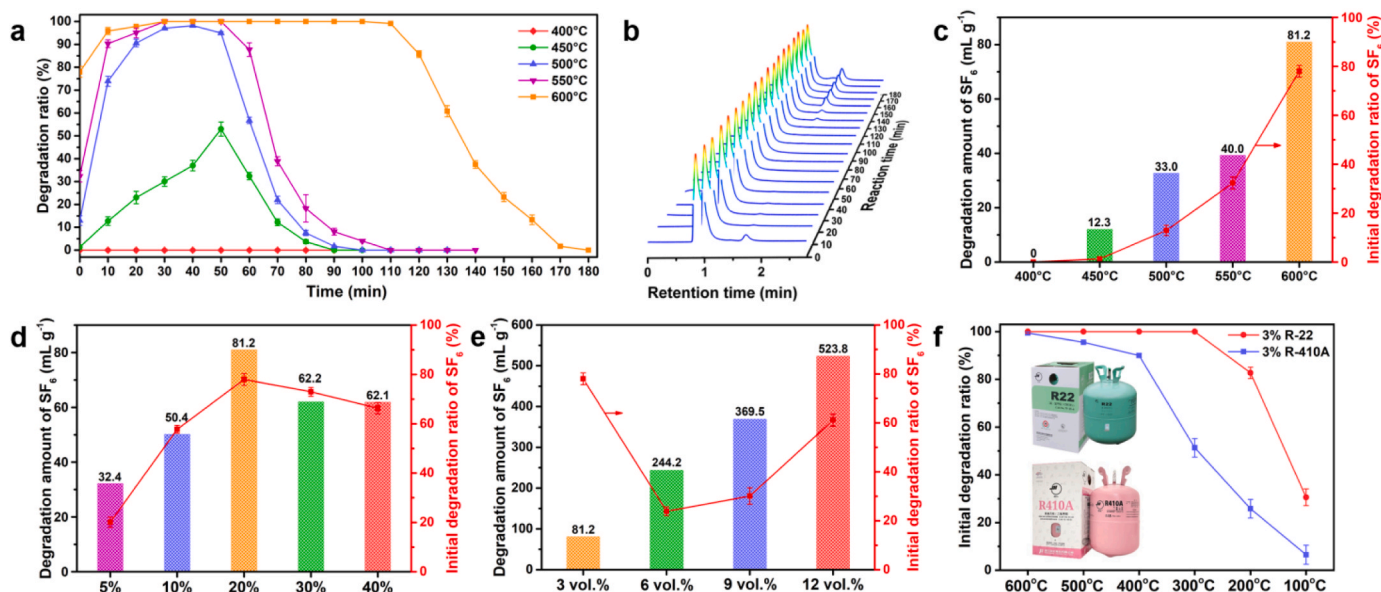
Fig. 5. . a-c) The effect of different temperatures (400 °C, 450 °C, 500 °C, 550 °C, and 600 °C) on SF_6 degradation; The effect of d) different Mn content in composites (5 wt%, 10 wt%, 20 wt%, 30 wt%, and 40 wt%), e) different SF_6 concentrations (3 vol%, 6 vol%, 9 vol% and 12 vol%); f) Degradation performance to R-22 ($CHClF_2$) and R-410A (50%CH_2F_2/50%CF_3CHF_2). When exploring the effect of different experimental parameters (sample, temperature, metal active centers, Mn content in composites, and flow rate), change only one type of factor at a time.

4. Conclusions

In summary, herein, we introduced a simple and low-cost method to fabricate the MnOx@Mn/SiC heterojunction and improved the catalytic degradation activity of SF_6. Due to the strong electron coupling driven by different work functions, MnOx@Mn species transferred electrons to SiC, thus forming the SiO(δ^-) /MnO(δ^+) heterojunction interface. MnO (δ^+), acting as an electron donor, facilitated the adsorption and activation of SF_6 molecules. Therefore, the MnOx@Mn/SiC heterojunction with spontaneous electron transfer has better performance, which the degraded temperature can lower to 450 °C and the maximum degradation amount can reach 523.8 mL g^{-1}. The evolution of the active-phase during the reaction was characterized by in-situ XRD, which confirmed the existence of Mn_2O_3 intermediates at high temperature. In addition to SF_6, MnOx@Mn/SiC also has excellent ability to fix other electronegative gases at low temperatures, such as R-22 and R-410A, which have global warming potential of 2090 and 1989 CO_2 equivalent, respectively. Such a heterojunction catalytic system with spontaneous electron transfer provides a new strategy for the adsorption and activation of inert small molecules, thus solving the effective fixation of electronegative F-gases with strong greenhouse effect.

CRediT authorship contribution statement

Meng Xiang: Conceptualization, Data curation, Investigation, Methodology, Writing – original draft, Writing – review & editing. **Dong Boxu:** Methodology, Software, Writing – review & editing. **Zhao Liang:** Investigation, Validation, Writing – review & editing. **Zhou Wenhui:** Investigation, Writing – review & editing. **Li Xinhao:** Methodology, Supervision, Writing – review & editing. **Zai Jiantao:** Conceptualization, Formal analysis, Funding acquisition, Methodology, Resources, Supervision, Writing – original draft, Writing – review & editing. **Qian Xuefeng:** Funding acquisition, Supervision, Validation, Visualization, Writing – review & editing.

Declaration of Competing Interest

The authors declare that they have no known competing financial interests or personal relationships that could have appeared to influence the work reported in this paper.

Data Availability

Data will be made available on request.

Appendix A. Supporting information

Supplementary data associated with this article can be found in the online version at doi:10.1016/j.apcatb.2024.123709.

References

[1] T. Hasell, M. Miklitz, A. Stephenson, M.A. Little, S.Y. Chong, R. Clowes, L. Chen, D. Holden, G.A. Tribello, K.E. Jelfs, Porous organic cages for sulfur hexafluoride separation, J. Am. Chem. Soc. 138 (2016) 1653–1659.

[2] S.A. Montzka, E.J. Dlugokencky, J.H. Butler, Non-CO_2 greenhouse gases and climate change, Nature 476 (2011) 43–50.

[3] S.M. Wang, X.T. Mu, H.R. Liu, S.T. Zheng, Q.Y. Yang, Pore-structure control in metal–organic frameworks (MOFs) for capture of the greenhouse gas SF_6 with record separation, Angew. Chem. 134 (2022) e202207066.

[4] A. Ravishankara, S. Solomon, A.A. Turnipseed, R. Warren, Atmospheric lifetimes of long-lived halogenated species, Science 259 (1993) 194–199.

[5] B.K. Sovacool, S. Griffiths, J. Kim, M. Bazilian, Climate change and industrial F-gases: a critical and systematic review of developments, sociotechnical systems and policy options for reducing synthetic greenhouse gas emissions, Renew. Sustain. Energy Rev. 141 (2021) 110759.

[6] Y. Bo, K. Ross, Z. Jingjing, K. Igusky, S. Ranping, T. Damassa, Opportunities to enhance non-carbon dioxide greenhouse gas mitigation in China, World Resour. Inst. (2016) 1–40.

[7] R. Sun, C.-W. Tai, M. Strømme, O. Cheung, Hierarchical porous carbon synthesized from novel porous amorphous calcium or magnesium citrate with enhanced SF_6 uptake and SF_6/N_2 selectivity, ACS Appl. Nano Mater. 2 (2019) 778–789.

[8] J. Ren, M. Chang, W. Zeng, Y. Xia, D. Liu, G. Maurin, Q. Yang, Computer-aided discovery of MOFs with calixarene-analogous microenvironment for exceptional SF_6 capture, Chem. Mater. 33 (2021) 5108–5114.

[9] C.Y. Chuah, Y. Lee, T.-H. Bae, Potential of adsorbents and membranes for SF_6 capture and recovery: a review, Chem. Eng. J. 404 (2021) 126577.

[10] Q. Liao, C. Ke, X. Huang, D. Wang, Q. Han, Y. Zhang, Y. Zhang, K. Xi, A versatile method for functionalization of covalent organic frameworks via Suzuki–Miyaura cross-coupling, Angew. Chem. 133 (2021) 1431–1436.

[11] Y. Gutierrez, M.M. Giangregorio, F. Palumbo, F. Gonzalez, A.S. Brown, F. Moreno, M. Losurdo, Sustainable and tunable Mg/MgO Plasmon-catalytic platform for the grand challenge of SF_6 environmental remediation, Nano Lett. 20 (2020) 3352–3360.

[12] J. Zhang, J.Z. Zhou, Z.P. Xu, Y. Li, T. Cao, J. Zhao, X. Ruan, Q. Liu, G. Qian, Decomposition of potent greenhouse gas sulfur hexafluoride (SF_6) by Kirschsteinite-dominant stainless steel slag, Environ. Sci. Technol. 48 (2014) 599–606.

[13] D. Kolodko, I. Sorokin, V. Tarakanov, E. Shustin, Model of a plasma layer formed by an electron beam, Plasma Phys. Rep. 46 (2020) 703–708.

[14] L. Huang, Y. Shen, W. Dong, R. Zhang, J. Zhang, H. Hou, A novel method to decompose two potent greenhouse gases: Photoreduction of SF_6 and SF_5CF_3 in the presence of propene, J. Hazard. Mater. 151 (2008) 323–330.

[15] J. Wu, J. Zhang, Z. Cao, Q. Liu, F. Wei, J. Zhou, D. Wang, S. Shi, G. Qian, Improvement on fluorine migration from SF_6 to SiF_4 by an efficient mediator of Fe_2O_3/Cr_2O_3 composites, ACS Appl. Mater. Interfaces 11 (2019) 16538–16545.

[16] S. Li, P. Wu, J.E. Moses, K.B. Sharpless, Multidimensional SuFEx click chemistry: sequential sulfur (VI) fluoride exchange connections of diverse modules launched from an SOF_4 hub, Angew. Chem. 129 (2017) 2949–2954.

[17] D. Ma, B. Hu, W. Wu, X. Liu, J. Zai, C. Shu, T. Tadesse Tsega, L. Chen, X. Qian, T. L. Liu, Highly active nanostructured CoS_2/CoS heterojunction electrocatalysts for aqueous polysulfide/iodide redox flow batteries, Nat. Commun. 10 (2019) 3367.

[18] M. Yuan, J. Chen, Y. Bai, Z. Liu, J. Zhang, T. Zhao, Q. Wang, S. Li, H. He, G. Zhang, Unveiling electrochemical urea synthesis by Co-activation of CO_2 and N_2 with Mott–Schottky heterostructure catalysts, Angew. Chem. 133 (2021) 11005–11013.

[19] L.H. Sun, Q.Y. Li, S.N. Zhang, D. Xu, Z.H. Xue, H. Su, X. Lin, G.Y. Zhai, P. Gao, S. I. Hirano, Heterojunction-based electron donors to stabilize and activate ultrafine Pt nanoparticles for efficient hydrogen atom dissociation and gas evolution, Angew. Chem. 133 (2021) 25970–25974.

[20] K. He, T. Tadesse Tsega, X. Liu, J. Zai, X.H. Li, X. Liu, W. Li, N. Ali, X. Qian, Utilizing the Space-Charge region of the FeNi-LDH/CoP P-n junction to promote performance in oxygen evolution electrocatalysis, Angew. Chem., Int. Ed. 58 (2019) 11903–11909.

[21] R. Qin, L. Zhou, P. Liu, Y. Gong, K. Liu, C. Xu, Y. Zhao, L. Gu, G. Fu, N. Zheng, Alkali ions secure hydrides for catalytic hydrogenation, Nat. Cata 3 (2020) 703–709.

[22] T. Stahl, H.F. Klare, M. Oestreich, Main-group Lewis acids for C–F bond activation, ACS Catal. 3 (2013) 1578–1587.

[23] L. Köring, A. Stepen, B. Birenheide, S. Barth, M. Leskov, R. Schoch, F. Krämer, F. Breher, J. Paradies, Boron-centered Lewis superacid through Redox-active ligands: application in C-F and S-F bond activation, Angew. Chem., Int. Ed. 62 (2023) e202216959.

[24] S. Yoshida, K. Shimomori, Y. Kim, T. Hosoya, Single C-F bond cleavage of trifluoromethylarenes with an ortho-Silyl group, Angew. Chem. 128 (2016) 10562–10565.

[25] K. Chen, N. Berg, R. Gschwind, B. König, Selective single C(sp3)–F bond cleavage in trifluoromethylarenes: merging visible-light catalysis with Lewis acid activation, J. Am. Chem. Soc. 139 (2017) 18444–18447.

[26] H. Kameo, H. Yamamoto, K. Ikeda, T. Isasa, S. Sakaki, H. Matsuzaka, Y. García-Rodeja, K. Miqueu, D. Bourissou, Fluorosilane activation by Pd/Ni→ Si–F→ Lewis acid interaction: an entry to catalytic Sila-Negishi coupling, J. Am. Chem. Soc. 142 (2020) 14039–14044.

[27] X. Meng, J. Hu, B. Dong, Y. Zhu, Y. Zhang, J. Zai, X. Qian, Rectified $SiC-Fe_2O_3$ heterostructures for high efficient activation and degradation of sulfur hexafluoride in air atmosphere, Chem. Eng. J. 450 (2022) 137949.

[28] H. Xiong, M.H. Wiebenga, C. Carrillo, J.R. Gaudet, H.N. Pham, D. Kunwar, S.H. Oh, G. Qi, C.H. Kim, A.K. Datye, Design considerations for low-temperature hydrocarbon oxidation reactions on Pd based catalysts, Appl. Catal. B: Environ. 236 (2018) 436–444.

[29] R. Gao, M. Zhang, Y. Liu, S. Xie, J. Deng, X. Ke, L. Jing, Z. Hou, X. Zhang, F. Liu, Engineering platinum catalysts via a site-isolation strategy with enhanced chlorine resistance for the elimination of multicomponent VOCs, Environ. Sci. Technol. 56 (2022) 9672–9682.

[30] Y. Zheng, Y. Su, C. Pang, L. Yang, C. Song, N. Ji, D. Ma, X. Lu, R. Han, Q. Liu, Interface-enhanced oxygen vacancies of CoCuOx catalysts In situ grown on monolithic Cu foam for VOC catalytic oxidation, Environ. Sci. Technol. 56 (2021) 1905–1916.

[31] S. Liu, H. Wang, S. Wang, Y. Dai, B. Liu, Y. Liu, F. Dang, K.J. Smith, X. Nie, S. Hou, Engineering morphology and Ni substitution of $Ni_xCo_{3-x}O_4$ spinel oxides to promote catalytic combustion of ethane: Elucidating the influence of oxygen defects, ACS Catal. 13 (2023) 4683–4699.

[32] X. Zhong, M. h Oubla, X. Wang, Y. Huang, H. Zeng, S. Wang, K. Liu, J. Zhou, L. He, H. Zhong, Boosting oxygen reduction activity and enhancing stability through structural transformation of layered lithium manganese oxide, Nat. Commun. 12 (2021) 3136.

[33] P. Wu, S. Dai, G. Chen, S. Zhao, Z. Xu, M. Fu, P. Chen, Q. Chen, X. Jin, Y. Qiu, Interfacial effects in hierarchically porous $\alpha-MnO_2/Mn_3O_4$ heterostructures promote photocatalytic oxidation activity, Appl. Catal. B: Environ. 268 (2020) 118418.

[34] C. He, Y. Wang, Z. Li, Y. Huang, Y. Liao, D. Xia, S. Lee, Facet engineered $\alpha-MnO_2$ for efficient catalytic ozonation of odor CH_3SH: oxygen vacancy-induced active centers and catalytic mechanism, Environ. Sci. Technol. 54 (2020) 12771–12783.

[35] G. Feng, S. Wang, S. Li, R. Ge, X. Feng, J. Zhang, Y. Song, X. Dong, J. Zhang, G. Zeng, Highly selective photoelectroreduction of carbon dioxide to ethanol over graphene/silicon carbide composites, Angew. Chem. 135 (2023) e202218664.

[36] S.-S. Liu, Y.-Y. Jin, Y. Han, J. Zhao, J. Ren, Highly stable and coking resistant Ce promoted Ni/SiC catalyst towards high temperature CO methanation, Fuel Process. Technol. 177 (2018) 266–274.

[37] P. Wang, F. Chang, W. Gao, J. Guo, G. Wu, T. He, P. Chen, Breaking scaling relations to achieve low-temperature ammonia synthesis through LiH-mediated nitrogen transfer and hydrogenation, Nat. Chem. 9 (2017) 64–70.

[38] Y. Liu, C. Ma, Q. Zhang, W. Wang, P. Pan, L. Gu, D. Xu, J. Bao, Z. Dai, 2D electron gas and oxygen vacancy induced high oxygen evolution performances for advanced Co_3O_4/CeO_2 nanohybrids, Adv. Mater. 31 (2019) 1900062.

[39] C. Huang, X. Miao, C. Pi, B. Gao, X. Zhang, P. Qin, K. Huo, X. Peng, P.K. Chu, Mo_2C/VC heterojunction embedded in graphitic carbon network: an advanced electrocatalyst for hydrogen evolution, Nano Energy 60 (2019) 520–526.

[40] X. Li, Y. Wang, J. Wang, Y. Da, J. Zhang, L. Li, C. Zhong, Y. Deng, X. Han, W. Hu, Sequential electrodeposition of bifunctional catalytically active structures in $MoO_3/Ni–NiO$ composite electrocatalysts for selective hydrogen and oxygen evolution, Adv. Mater. 32 (2020) 2003414.

[41] J. Guan, C. Li, J. Zhao, Y. Yang, W. Zhou, Y. Wang, G.-R. Li, FeOOH-enhanced bifunctionality in Ni_3N nanotube arrays for water splitting, Appl. Catal. B: Environ. 269 (2020) 118600.

[42] M. Tian, X. Guo, R. Dong, Z. Guo, J. Shi, Y. Yu, M. Cheng, R. Albilali, C. He, Insight into the boosted catalytic performance and chlorine resistance of nanosphere-like meso-macroporous $CrO_x/MnCo_3O_x$ for 1, 2-dichloroethane destruction, Appl. Catal. B: Environ. 259 (2019) 118018.

[43] R. Yin, J. Chen, J. Mi, H. Liu, T. Yan, L. Shan, J. Lang, J. Li, Breaking the activity–selectivity trade-off for simultaneous catalytic elimination of nitric oxide and chlorobenzene via $FeVO_4–Fe_2O_3$ interfacial charge transfer, ACS Catal. 12 (2022) 3797–3806.

[44] F. Zeng, X. Guo, X. Feng, R. Cai, Q. Yao, S. Zhang, J. Tang, Theoretical study of the interaction of SF_6 molecule on $Ti_3C_2T_x$ surfaces, Appl. Surf. Sci. 597 (2022) 153721.

[45] B. Li, Y. Wang, N. Jiang, L. An, J. Song, Y. Zuo, F. Ning, H. Shang, D. Xia, Electrolytic-anion-redox adsorption pseudocapacitance in nanosized lithium-free transition metal oxides as cathode materials for Li-ion batteries, Nano Energy 72 (2020) 104727.

[46] W. Chen, A comparative study on the performance and environmental characteristics of R410A and R22 residential air conditioners, Appl. Therm. Eng. 28 (2008) 1–7.

[47] M. Ito, C. Dang, E. Hihara, Thermal decomposition of lower-GWP refrigerants, (2014).

[48] K. Olie, R. Addink, M. Schoonenboom, Metals as catalysts during the formation and decomposition of chlorinated dioxins and furans in incineration processes, J. Air Waste Manag. Assoc. 48 (1998) 101–105.